Tribology Letters (2018) 66:20
https://doi.org/10.1007/s11249-017-0967-9

ORIGINAL PAPER

Size of the Plastic Zone Produced by Nanoscratching

Iyad Alabd Alhafez[1] · Carlos J. Ruestes[2] · Herbert M. Urbassek[1]

Received: 28 August 2017 / Accepted: 29 November 2017

Abstract
Nanoscratching of ductile materials creates plastic zones surrounding the scratch groove. We approximate the geometry of these zones by a semicylinder with its axis oriented along the scratch direction. The radius and the length of the cylinder, as well as the length of the dislocations in the network created quantify the plasticity generated. Using molecular dynamics simulations, we characterize the plastic zones in six metals with fcc, bcc, and hcp crystal structures. We find that the plastic zone sizes after scratch are comparable to those after indent. Due to dislocation reactions, the dislocation networks simplify, reducing the total length of dislocations. As a consequence, the average dislocation density in the plastic zone stays roughly constant. Individually, we find exceptions from this simple picture. Fcc metals show strong plastic activity, which even increases during scratch. The hcp metals on the other side show the least plastic activity. Here the plasticity may be strongly reduced during scratch and particularly during tip withdrawal.

Keywords Molecular dynamics · Nanoindentation · Scratching · Dislocations · Plasticity

1 Introduction

When a surface is scratched and a groove created, the material around the groove is strongly damaged due to the plasticity created during scratching. In the case of metals, the plastic material response is usually based on dislocation activity. We study here the question as to how far the plastic zone created by the scratch extends into the material.

This issue has previously been considered almost exclusively in the context of nanoindentation, which constitutes an important technique to study the plastic behavior of materials [1, 2]. Here, the size of the plastic zone is assumed to be hemispherical with a radius R_{pl}. This radius was observed to scale with the contact radius, a_{c}, of the indenter as

$$R_{\mathrm{pl}} = f a_c \,. \tag{1}$$

The *plastic zone size factor f* depends on the material and is of the order of $f = 0$–3.5 [3].

✉ Herbert M. Urbassek
urbassek@rhrk.uni-kl.de
http://www.physik.uni-kl.de/urbassek/

[1] Physics Department and Research Center OPTIMAS, University Kaiserslautern, Erwin-Schrödinger-Straße, 67663 Kaiserslautern, Germany

[2] CONICET and Facultad de Ciencias Exactas y Naturales, Universidad Nacional de Cuyo, 5500 Mendoza, Argentina

In recent years, molecular dynamics (MD) simulations have contributed strongly to an understanding of the details of dislocation nucleation and growth during indentation [4]. Recent MD studies [5, 6] on single-crystal indentation corroborated the dependence, Eq. (1), but pointed at a strong influence of the crystal lattice structure on *f*; this is plausible since the type and properties of dislocations depend strongly on the underlying crystal lattice.

MD simulations have also been used to study scratching of a surface with a spherical tip; both fcc [7–12] and bcc [13–17] metals have been investigated, but less frequently hcp [18] lattices. It has been found that the dislocation network generated by the indent may be simplified during scratch by dislocation reactions; on the other hand, the ongoing scratching extends the network on the tip front. The question arises to what extent the *f* factor of nanoindentation may be used to characterize also the size of the plastic zone generated under scratch.

In this paper, we investigate the plastic zone created by nanoscratching using MD simulations. In order to take the variety of lattice structures into account, we study three lattice types (fcc, bcc, and hcp) and choose two metallic elements for each type. We wish to explore to what extent the available knowledge on the plastic zone surrounding an indentation pit can be extended to characterize a scratch groove. In particular, does the dislocation network built up

Published online: 13 December 2017

during indentation become more complex during scratch, or does it simplify due to dislocation reactions? And—related to this question—is the dislocation density around the scratch groove of similar size as around the indentation pit?

2 Method

Figure 1 shows a schematic representation of the MD simulation system. It illustrates the configuration of the tip and the substrate crystal. The simulation consists of three parts: (1) nanoindentation, during which the indenter is pushed perpendicular into the substrate to a depth $d = 3$ nm; (2) scratching parallel to the surface at the same depth for a total length of $L = 10$ nm; and (3) retraction of the indenter: the indenter is moved out of the substrate to return to the initial height.

We study scratching of two fcc metals (Al and Cu), two bcc metals (Fe and Ta), and two hcp metals (Ti and Zr). In all cases, the substrate is a single crystal. In order to have comparable scratch situations, we choose a scratching geometry, in which the available slip systems provide pileup of material immediately to the front of the tip. Thus we choose the (001)[010] scratch geometry for fcc, (100)[$0\bar{1}\bar{1}$] for bcc, and a prismatic plane for hcp, ($01\bar{1}0$)[$2\bar{1}\bar{1}0$]. The scratch

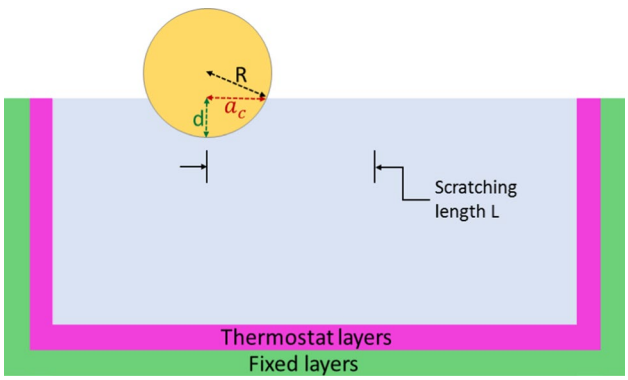

Fig. 1 Setup of the simulation system. The radius R of the indenter, its indentation depth d, the contact area radius a_c and the scratching length L are indicated. The substrate has thermostatting and rigid zones at its boundaries

geometries and the extensions of the simulation crystallites are assembled in Table 1. Here we made sure that the sizes were large enough to include the generated dislocations in the simulation volume.

The substrate interactions are chosen as follows. The Al–Al interaction is described by the Mendelev et al. [19] potential. For Cu we used the potential developed by Mishin et al. [20], for Fe the Mendelev et al. potential [21], and for Ta the Dai et al. potential [22]. Finally we used the potential by Mendelev et al. [23] for Ti, and the recent potential by Bertolino et al. [24] for Zr, which improves on a previous version [25].

We fix two atom layers at the bottom and at the side faces of the substrate in order to suppress any rigid-body movement of the substrate. The next four layers at the bottom and the sides are thermostatted to keep the temperature below 1 K in the simulation in order to avoid heating up of the material during machining; in addition, such a low temperature is chosen to rule out thermally activated mechanisms.

After performing a series of preliminary simulations, we chose the system size large enough that the dislocation network adherent to the indent and scratch groove do not approach the boundaries. However, emitted dislocation loops can travel far, and it is not possible in an MD simulation to avoid their interaction with the boundaries. Previous MD simulation work [6, 26–28] studied this influence. In short, fixed boundaries, such as those used here, tend to reflect emitted loops back into the simulation volume, while free boundaries absorb the loops. It is not straightforward to decide which boundaries are closer to reality; this feature depends on dislocation mobility and on the density of defects in the crystals used in experiment, which could pin dislocation loops.

Before performing the simulations, the substrates are relaxed until all stress components have reached values $< 10^{-5}$ GPa [29]. The tip velocity is chosen as 20 m/s, both for indentation and scratching. This velocity, though high compared to experimental indentation and scratching velocities, is within the range of a few per mille of the longitudinal wave velocity of each of the metals probed, and should be considered low enough for typical MD studies. We note that the effect of tip velocity has been studied in particular

Table 1 Crystals used in the simulation, their orientations, the respective dimensions of the workpiece in the same order, and the number of atoms

Crystal	Surface orientation	Scratch direction	Lateral direction	Dimensions (nm)	Number of atoms
Al	[001]	[010]	[100]	$49 \times 66 \times 56$	11.0×10^6
Cu	[001]	[010]	[100]	$49 \times 66 \times 56$	15.2×10^6
Fe	[100]	[$0\bar{1}\bar{1}$]	[$0\bar{1}1$]	$36 \times 66 \times 56$	11.4×10^6
Ta	[100]	[$0\bar{1}\bar{1}$]	[$0\bar{1}1$]	$50 \times 65 \times 56$	10.0×10^6
Ti	[$01\bar{1}0$]	[$2\bar{1}\bar{1}0$]	[0001]	$49 \times 66 \times 57$	10.5×10^6
Zr	[$01\bar{1}0$]	[$2\bar{1}\bar{1}0$]	[0001]	$48 \times 66 \times 56$	7.6×10^6

by MD simulations of indentation. Such simulations were performed for fcc Al with velocities in the range of 0.004–4 m/s [30]; for bcc Fe and Ta the velocity was varied between 3 and 100 m/s [5, 31]. These simulations showed no significant influence of velocity; only for the highest velocity (100 m/s) dislocation nucleation was found to be substantially suppressed. Simulational tests of the influence of scratch speed are more rare. Li et al. [32, 33] investigated the influence of the cutting speed for fcc Cu, but only for speeds above 25 or even 50 m/s; not surprisingly, they report increased workpiece heating at higher speeds.

The tip has a spherical shape with a radius of $R = 5$ nm. It interacts in a purely repulsive way with the substrate atoms according to the law [34]

$$V(r) = \begin{cases} k(R-r)^3, & r < R, \\ 0, & r \geq R. \end{cases} \tag{2}$$

Here r is the distance of a substrate atom to the center of the indenter, and $k = 10$ eV/Å^3 [34, 35] is a constant. For the indenter model chosen, there are no tangential forces, as appropriate for a Hertzian indenter.

The MD simulations are performed using the open-source LAMMPS code [36] with a constant time step of 1 fs. The software tools OVITO [37] and Paraview [38] are used for visualization of the results; DXA [39] and CAT [40–42] are employed for analysis of the dislocations generated.

In previous work [5, 6] the plastic zone generated by nanoindentation was described as a hemisphere centered on the indent point, see Fig. 2a. The radius of the hemisphere, R_{pl}, was determined as the largest distance of a dislocation line to the indent point. Note that emitted dislocation loops, i.e., loops that have lost contact with the dislocation network adherent to the indent zone, are not included in this procedure. The average dislocation density in the plastic zone can be obtained by dividing the length of the dislocation lines in the adherent network, $L^{\mathrm{adh}}_{\mathrm{disl}}$, by the volume of the hemisphere after correcting for the indentation volume.

We proceed analogously for the case of scratching, see Fig. 2b. The plastic zone is approximated as a semicylinder with the scratch direction as its axis. The length of the cylinder is given by the distance between the front and rear ends of the dislocation network, Z. R_{pl} now describes the cylinder radius, and the average dislocation density is given by

$$\bar{\rho} = \frac{L^{\mathrm{adh}}_{\mathrm{disl}}}{V_{\mathrm{cyl}} - V_{\mathrm{groove}}}, \tag{3}$$

where $V_{\mathrm{cyl}} = \frac{\pi}{2} R^2_{\mathrm{pl}} Z$ is the volume of the semicylinder and V_{groove} is the volume of the scratch groove. A plastic size factor, f, was calculated from R_{pl} according to Eq. (1).

We note that dislocations do not fill homogeneously the hemispherical (for indentation), or cylindrical (for scratch), plastic zone as defined by us. This is due both to the crystalline anisotropy of the dislocation generation and propagation process and to the discrete atomistic nature of the dislocations themselves; both features are well captured by our atomistic simulations. The 'true' shape of the plastic zone—if it could be defined—would look rather irregular. It would not only depend on the crystal orientation during scratch but would also change for each individual scratch due to the statistical nature of dislocation nucleation. As a consequence, our estimate of the plastic volume overestimates the true volume; analogously our estimate of the dislocation density, Eq. (3), is an underestimate.

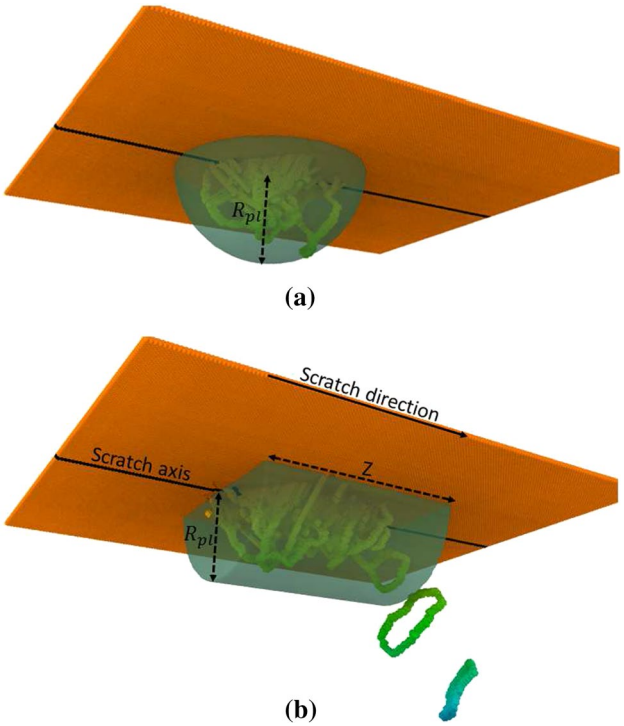

Fig. 2 Definition of the plastic zone radius, R_{pl}, for **a** indention and **b** scratch. Z indicates the distance between the front and rear ends of the dislocation network

3 Results

3.1 Forces

The determination of the forces acting on the tip during scratching is straightforward in an MD simulation. Figure 3 displays the evolution of the normal and tangential forces during scratching. The normal force, F_{norm}, is required to keep the tip at its prescribed depth, d, while the tangential force, F_{tang}, is used to plow the tip through the substrate.

For an assessment of the forces, a knowledge of the material hardness using the interaction potentials is helpful, such

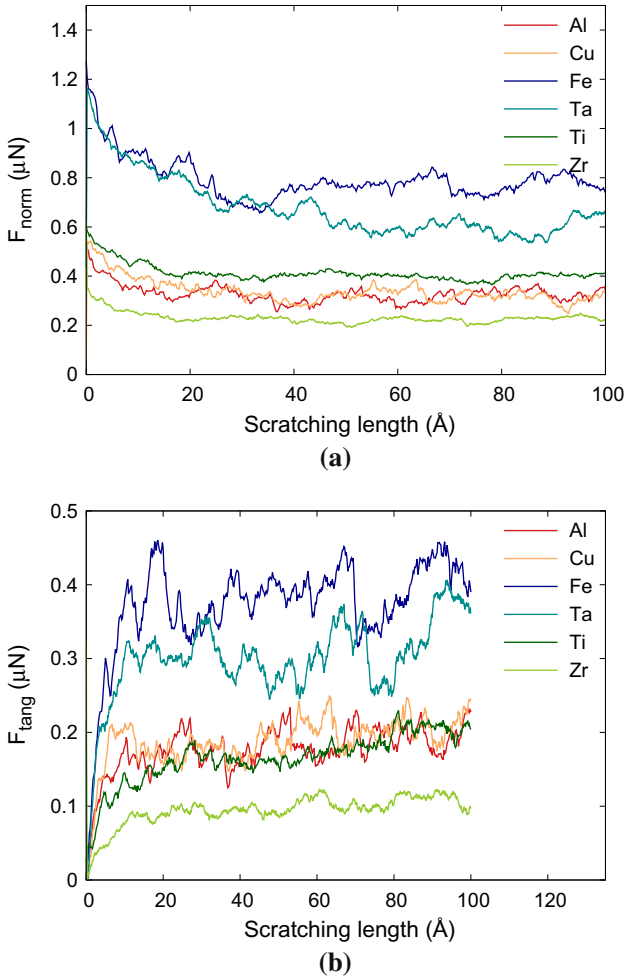

Fig. 3 Evolution of the **a** normal and **b** tangential force during scratch

as it is obtained from an indentation simulation. Thus we note that Cu (12 GPa) is harder than Al (6 GPa) [29], while the bcc materials Fe (18 GPa) [17] and Ta (16–20 GPa) [31] have similar hardness. Finally, Ti exhibits a hardness of 6.6 GPa [18] while we determine the hardness of Zr in the Bertolino et al. potential [24] used here to 5.3 GPa. We note that for the determination of hardness values from MD simulations, an appropriate determination of the contact areas is essential. These areas may be determined by counting the substrate atoms that are in contact with the tip and summing over the (projected) areas of the contact atoms. Details of the procedure are provided in Refs. [16, 29].

The normal forces show a generally decreasing trend during the first 40 Å of scratching. It is caused by the changing contact geometry of the tip; while after indent the tip has a circular contact area, it develops to a semicircle during scratch, as the rear part of the tip loses contact with the substrate [15, 17, 18]. During this run-in phase of the first 40 Å, the tangential forces build up from their initial value of zero after indent to their final value

Table 2 Average normal force, F_{norm}, tangential force, F_{tang}, and friction coefficient, μ, during scratching the six metals investigated

Crystal	F_{norm} (μN)	F_{tang} (μN)	μ
Al	0.31	0.19	0.61
Cu	0.33	0.19	0.57
Fe	0.77	0.39	0.51
Ta	0.61	0.31	0.51
Ti	0.40	0.18	0.45
Zr	0.22	0.10	0.45

The averages are taken over the last 6 nm of the scratch

during scratch. The tangential forces show similarly strong fluctuations as the normal forces, in particular for the bcc materials. For the example of Fe, we can observe that fluctuations in F_{norm} and F_{tang} are correlated, see for instance the peak at 20 Å scratching length; the common origin of these excursions is the generation of dislocations. Since the bcc materials are the hardest, the generation of dislocations requires the highest forces; this also explains the larger fluctuations observed for this class of materials. Note that F_{tang} shows a generally increasing linear trend even after the run-in phase; this is particularly well seen for the less fluctuating fcc and hcp materials and is caused by the developing frontal crater rim, which leads to a larger amount of material which needs to be displaced while scratching.

We average the forces after the run-in phase and display the results in Table 2. The forces are systematically highest for the bcc materials, and here somewhat higher for Fe than for Ta, in correspondence with the larger hardness of bcc metals mentioned above. The fcc and hcp materials have comparable values. Zr shows particularly small forces in accordance with its small hardness.

We obtain a friction coefficient

$$\mu = \frac{F_{\text{tang}}}{F_{\text{norm}}} \tag{4}$$

from these data and display it in Table 2. The friction coefficient shows more uniformity than the absolute forces; the hcp metals have lowest coefficients of 0.45, followed by the bcc materials ($\mu = 0.51$). The fcc metals exhibit the highest coefficient of around 0.6.

In a simple geometrical model of plowing friction [43], μ is independent of the material and only depends on the form of the tip. Indeed this model assumes that the material hardness is a constant characterizing equally the normal and the tangential force. Then Eq. (4) simplifies to $\mu = A_{\text{tang}}/A_{\text{norm}}$, where A_{tang} (A_{norm}) are the tangential and normal projected tip areas; the friction coefficient only depends on the form of the tip and the scratch depth, but

not on the material. In more modern language, plowing requires the generation of the same amount of geometrically necessary dislocations for every material under the same deformation. This simple model does obviously not hold in our case.

In real materials, the situation is more complex due (1) to the availability of slip systems, and (2) to the energetic cost of creating dislocations. The second issue can be quantified by the stacking fault energy (SFE); we compile them for the materials used here in Table 3. Here indeed, fcc metals have generally smaller SFEs than the hcp metals; this is in agreement both with the length of dislocations observed—see Fig. 5a—and the friction coefficient. The SFE of bcc metals is so high that dislocations usually do not dissociate; however, the length of dislocations generated is similar to that of the hcp materials, and so are the friction coefficients.

Table 3 Stacking fault energies (SFE) for the materials investigated; if values are known for several planes, they are listed

Crystal	SFE (mJ/m^2)	References
Al	144–162	[44, 45]
Cu	44.4	[20]
Fe	670–960 ({110})	[46, 47]
Ta	700–850	[31]
Ti	118 (basal), 255 (prismatic)	[23]
Zr	70 (basal), 162 (prismatic)	[24]

If available, data are provided for the potentials used here

3.2 Plastic Zone

3.2.1 After Indentation

In this section, we characterize the dislocation network created by scratching. To this end, Fig. 4 provides snapshots of the plastic zones as created after the indent. At first sight, the structure of the dislocation networks looks quite similar for the six metals studied, in that a dense dislocation network surrounds the indent pit. All fcc and hcp metals emit dislocation loops; one of them, which is still quite close to the adherent network, is seen for Cu in Fig. 4. These loops move out of the indentation zone due to the strong stress that has built up there. We assemble the quantitative characteristics—the total length of the indentation network, $L_{\mathrm{disl}}^{\mathrm{adh}}$, and the average dislocation density, $\bar{\rho}$—in Table 4. There we see that the density reaches values characteristic of strongly cold-worked metals, in the range of several 10^{16} m^{-2}.

In detail, we observe that the fcc metals build up the largest networks; in particular Cu shows the highest $L_{\mathrm{disl}}^{\mathrm{adh}}$. Indeed, Cu has a lower SFE energy than Al, cf. Table 3, and so a multitude of partials and stacking faults are formed for this material.

The network in fcc materials is mainly built of $\frac{1}{6}\langle 211\rangle$ partials. In bcc metals, $\frac{1}{2}\langle 111\rangle$ dislocations are most prominent; these may form long semi-loops that at a later stage may also be emitted by what has been termed the 'lasso' mechanism [31]. Finally, in the hcp metals, the perfect $\frac{1}{3}\langle \bar{2}110\rangle$ dislocations and their partials $\frac{1}{3}\langle \bar{1}100\rangle$ are dominant. These

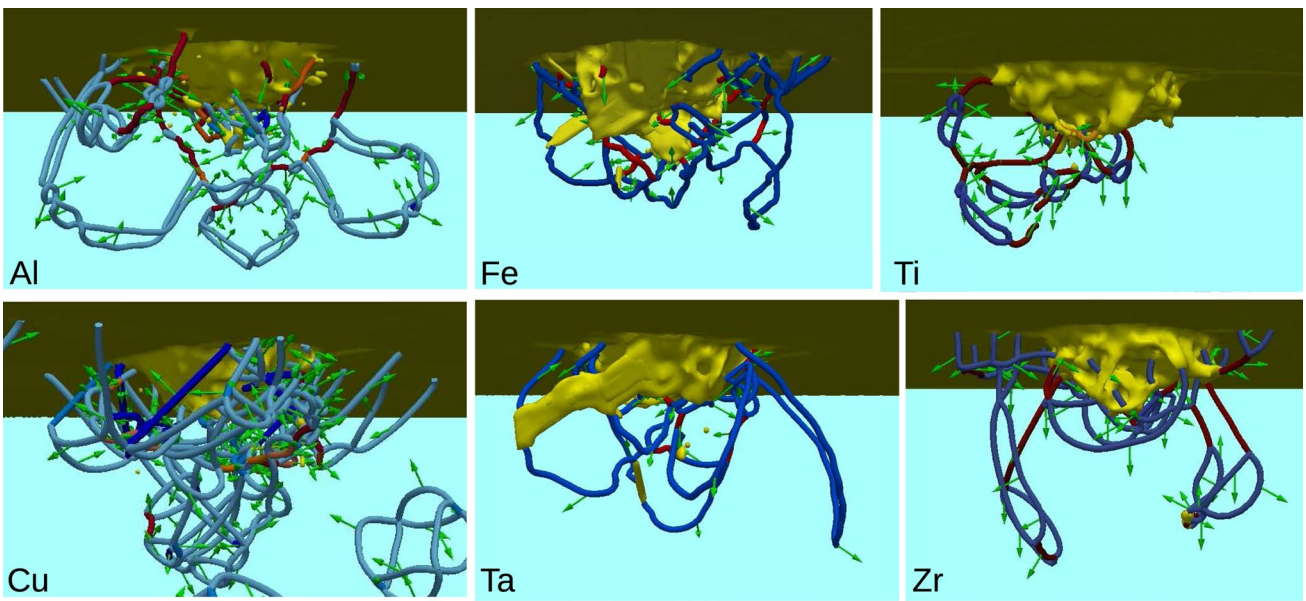

Fig. 4 Snapshots showing the dislocation networks after indent for the six metals investigated. Yellow: deformed surface and other unidentified defects. Dislocations are colored according to their Burgers vector $\boldsymbol{b}$. Fcc: light blue $\frac{1}{6}\langle 211\rangle$, dark blue $\frac{1}{6}\langle 110\rangle$, red $\frac{1}{2}\langle 110\rangle$, orange $\frac{1}{3}\langle 110\rangle$. Bcc: blue $\frac{1}{2}\langle 111\rangle$, red $\langle 100\rangle$. Hcp: blue $\frac{1}{3}\langle \bar{1}100\rangle$, red $\frac{1}{3}\langle \bar{2}110\rangle$, orange $\frac{1}{6}\langle \bar{2}203\rangle$, white $= \frac{1}{2}\langle 0001\rangle$

Table 4 Characteristics of the plastic zone after indent, after scratch, and after retraction

Crystal	After indent				After scratch					After retraction				
	R_{pl} (Å)	f	L_{disl}^{adh} (Å)	$\bar{\rho}$ (10^{16} m^{-2})	Z (Å)	R_{pl} (Å)	f	L_{disl}^{adh} (Å)	$\bar{\rho}$ (10^{16} m^{-2})	Z (Å)	R_{pl} (Å)	f	L_{disl}^{adh} (Å)	$\bar{\rho}$ (10^{16} m^{-2})
Al	153	3.3	3136	4.24	235	130	2.8	4720	7.92	165	130	2.8	2609	6.36
Cu	160	3.5	5044	5.89	303	138	3.1	7080	8.0	181	138	3.1	6976	8.5
Fe	118	2.6	1652	4.96	262	108	2.4	2376	5.25	255	109	2.4	1698	4.33
Ta	163	3.6	1609	1.81	217	138	3.1	1639	2.6	215	126	2.8	1224	2.3
Ti	119	2.6	1075	3.15	233	78	1.7	1394	7.15	25	25	0.5	137	55.82
Zr	159	3.5	1892	2.30	222	84	1.9	2483	10.0	212	75	1.6	126	0.72

R_{pl} radius of plastic zone, Z length of the plastic zone, f plastic zone size factor, L_{disl}^{adh} total dislocation length within plastic zone, $\bar{\rho}$ average dislocation density

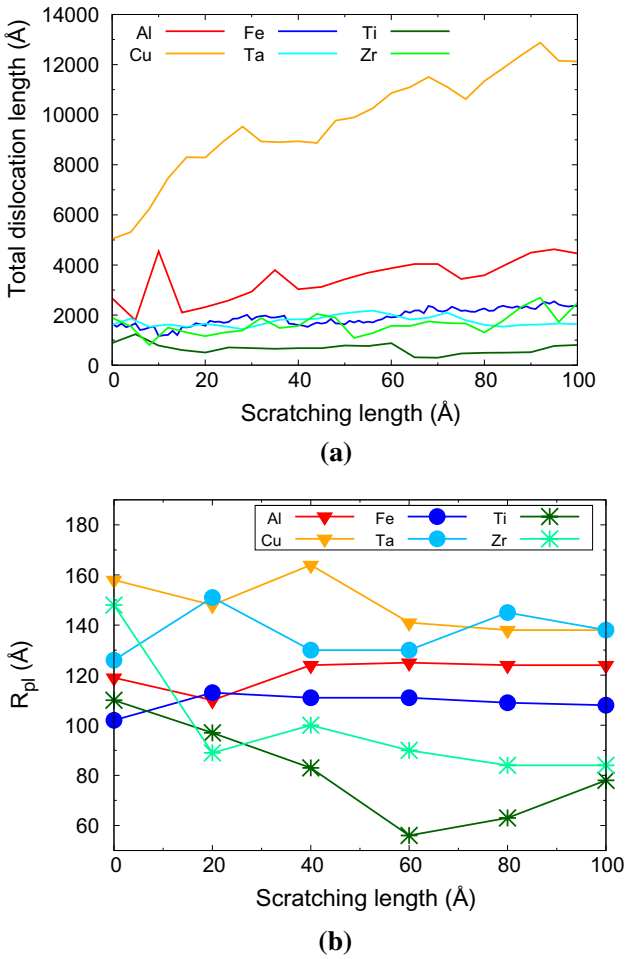

Fig. 5 Evolution of the **a** length of the dislocation network, L_{disl}^{adh}, and of the **b** plastic zone radius, R_{pl}, during scratch

also may lead to loop emission [6]; the extended semi-loops showing up for Zr already point in this direction.

The plastic zone size factor, Eq. (1), shows rather consistent values of $f = 2.6$–3.6, see Table 4. This is in agreement with previous findings of MD results of the plastic zone structure in these three crystal classes [5, 6]. The largest values are found for Cu, Ta, and Zr, and are due to the fact that here the dislocation network has evolved to reach the state of loop emission.

3.2.2 Evolution During Scratch

Figure 5 quantifies the evolution of the dislocation network during scratch. The length of the network, L_{disl}^{adh}, shows a more or less monotonically increasing trend for all materials; this trend is most strong for the fcc materials. The fluctuations superimposed are due to dislocation reactions simplifying the network. The plastic zone radius, Fig. 5b, similarly shows strong fluctuations. For the bcc materials, and also for the fcc Al, R_{pl} appears to show a constant trend below these fluctuations; while for Cu the plastic zone radius appears to shrink somewhat. The shrinking is most pronounced for both hcp metals investigated; here the plastic zone radius after indentation decreases strongly during scratch.

3.2.3 After Scratch

In order to understand in more detail the evolution of the plasticity, we study the details of the dislocation network.

The dislocation networks immediately after scratch, and after retraction of the indenter are displayed in Fig. 6a, b, respectively; the pertinent quantitative results are assembled in Table 4. Here quite strong differences between the three crystal classes show up.

The fcc materials build up a complex network. As shown in Table 4, the dislocation density actually increases for these metals. The plastic zone radius slightly decreases as compared to the after-indent situation; but the values of $f = 2.8$ and 3.1 are still in a comparable range. Dislocation reactions lead to a larger fraction of additional dislocations showing up, such as $\frac{1}{6}\langle 110\rangle$, $\frac{1}{2}\langle 110\rangle$, and $\frac{1}{3}\langle 110\rangle$. Tip retraction—during which the stress field created by the tip load and the material presence of the tip are removed—leads to some simplification of the network in the case of Al, but not in the case of Cu. In that latter case the dislocation density

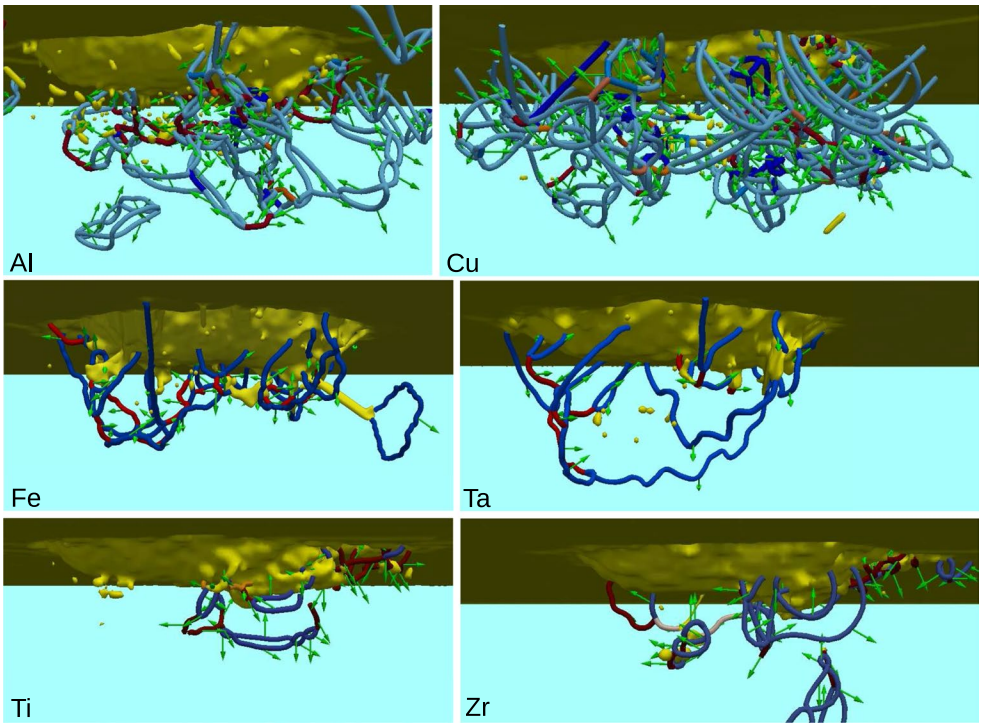

(a)

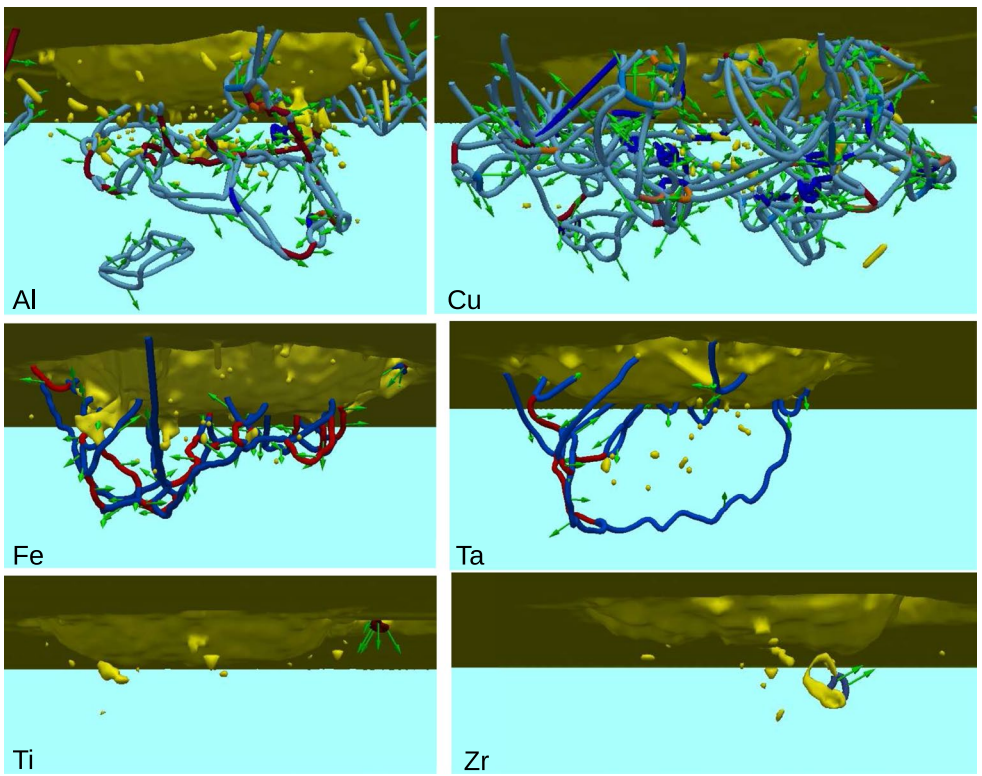

(b)

Fig. 6 Snapshots showing the dislocation networks **a** after scratch and **b** after removal of the tip for the six metals investigated. Dislocations are colored as in Fig. 4

even increases; this is caused by the strong reduction in the plastic cylinder length, Z, upon tip reduction.

In these materials, plasticity is dominated by Shockley partials and by Lomer–Cottrell locks that form by reactions of the type $\frac{1}{6}[112] + \frac{1}{6}[11\bar{2}] \rightarrow \frac{1}{3}[110]$. This sessile dislocation, also known as a stair-rod dislocation, contributes to strain hardening by impeding slip in the (111) and $(11\bar{1})$ plane, acting as a barrier for any additional dislocation moving in these planes. To a lesser amount, also perfect dislocations were identified. A few Frank partial dislocations, $\boldsymbol{b} = \frac{1}{3}[111]$, were found as well, which constitute another type of sessile dislocation in fcc metals.

In the bcc metals, a more pronounced simplification of the network can be observed during scratching. The total length of the network is only 30–60% of that in the fcc cases. This is caused by the large variety of partials available in fcc, but not in bcc, materials. Partial dislocations have a smaller Burgers vector and hence can be created at less energetic cost than full dislocations. On the other hand, the reduction in the f factor during scratch is of a similar magnitude as for the fcc materials, resulting in $f = 2.4$–3.1 after scratch. Retraction of the indenter leads to a reduction in the dislocation network in the order of 25–30%; while the f factor slightly decreases, the average dislocation density does not change much and remains in the order of magnitude that was established already after indent.

During the scratching process, prismatic loops are punched out in the scratching direction. They result form the interaction of previously nucleated shear loops that cross-slip and react to form the prismatic loop, in a process denoted as the 'lasso mechanism' [48]. Our dislocation analysis also reveals the presence of $\langle 100 \rangle$ dislocations. Such dislocations have higher energy than $\frac{1}{2}\langle 111 \rangle$ dislocations, but are readily produced during scratching; indeed a recent study [15], where Fe scratching in the [110] direction was simulated, finds them in even higher abundance than the present study.

A quite different situation arises for the hcp materials. Here scratching leads to a considerable simplification of the network; in the case of Ti the network even retracts exclusively to the front part of the scratch, while the rear part is left dislocation-free. The length of the total dislocation network increased during scratch, mostly by loop emission; however, the plastic zone radius shrank considerably, since many dislocations adherent to the groove have been annihilated at the surface, such that the size factor is only $f = 1.7$–1.9. After tip retraction, both materials show almost no dislocations below the groove. An inspection of our MD results shows that with the vanishing of the stress field, most dislocations have been retracted to the surface and have been absorbed there. A similar collapse of the plastic zone in hcp was observed previously in studies of nanoindentation for both Ti and Zr [6], where in analogy to the present case the first prismatic plane was indented. We investigate the special feature of the complete reduction in the hcp dislocation network further in Appendix 1, where we discuss the depth dependence of scratching.

In these hcp materials, prismatic loops are produced with slip directions of $\langle \bar{2}110 \rangle$. The structure of such prismatic loops is rather complex, as it has components in multiple slip systems. For instance, there are components on the first-order prismatic planes, $\{10\bar{1}0\}$, along the $\langle 1\bar{2}10 \rangle$ direction, and also in the same direction but on the basal plane (0001). Loops in the basal plane dissociate due to the relatively low SFE, see Table 3; this feature explains the $\langle 1\bar{1}00 \rangle$ partials observed. The prismatic loops have another component which are slip traces occurring in $\{1011\}$ planes with $\langle 1\bar{2}10 \rangle$ direction. These are documented in the literature to be produced by high stress concentration [6, 49], and we are generating these dislocations with the high stress concentration of the indenter.

3.3 Groove

The grooves created in the pileups surrounding them are shown in Fig. 7a. Figure 7b assembles schematically the slip directions activated in our three crystal systems. In each case, there is a frontal slip system, but also lateral glide systems are activated. The frontal slip systems are essential for the pileups reaching maximum height at the scratch front, see Fig. 7. Since also glide systems transporting material laterally are partially activated, we see lateral groove rims in some cases, most pronouncedly for Al. Our simulation shows that in the case of Cu, lateral material transport is more directed downwards than upwards such that it does not contribute to the formation of lateral pileup at the groove; the situation is reverse for Al. This feature also explains the extremely high values of the dislocation density and of $L_{\mathrm{disl}}^{\mathrm{adh}}$ for Cu.

The height of the frontal pileup is usually around 30 Å, and thus comparable to the groove depth. Only for the bcc metals, the pileup reaches double this height. In fcc and hcp metals, most of the activated dislocations are partials that do not contribute to the pileup formation, while in bcc the predominant dislocations are of the $\frac{1}{2}\langle 111 \rangle$ type that forms the pileup.

4 Conclusions

In extension to previous work on the plastic zone created by indentation, we characterize the plastic zones created by nanoscratching. To this end, we approximate the plastic zones by a semicylinder with its axis oriented along the scratch direction. The radius, R_{pl}, and length, Z, of the cylinder characterize the geometry of the plastic zone, while

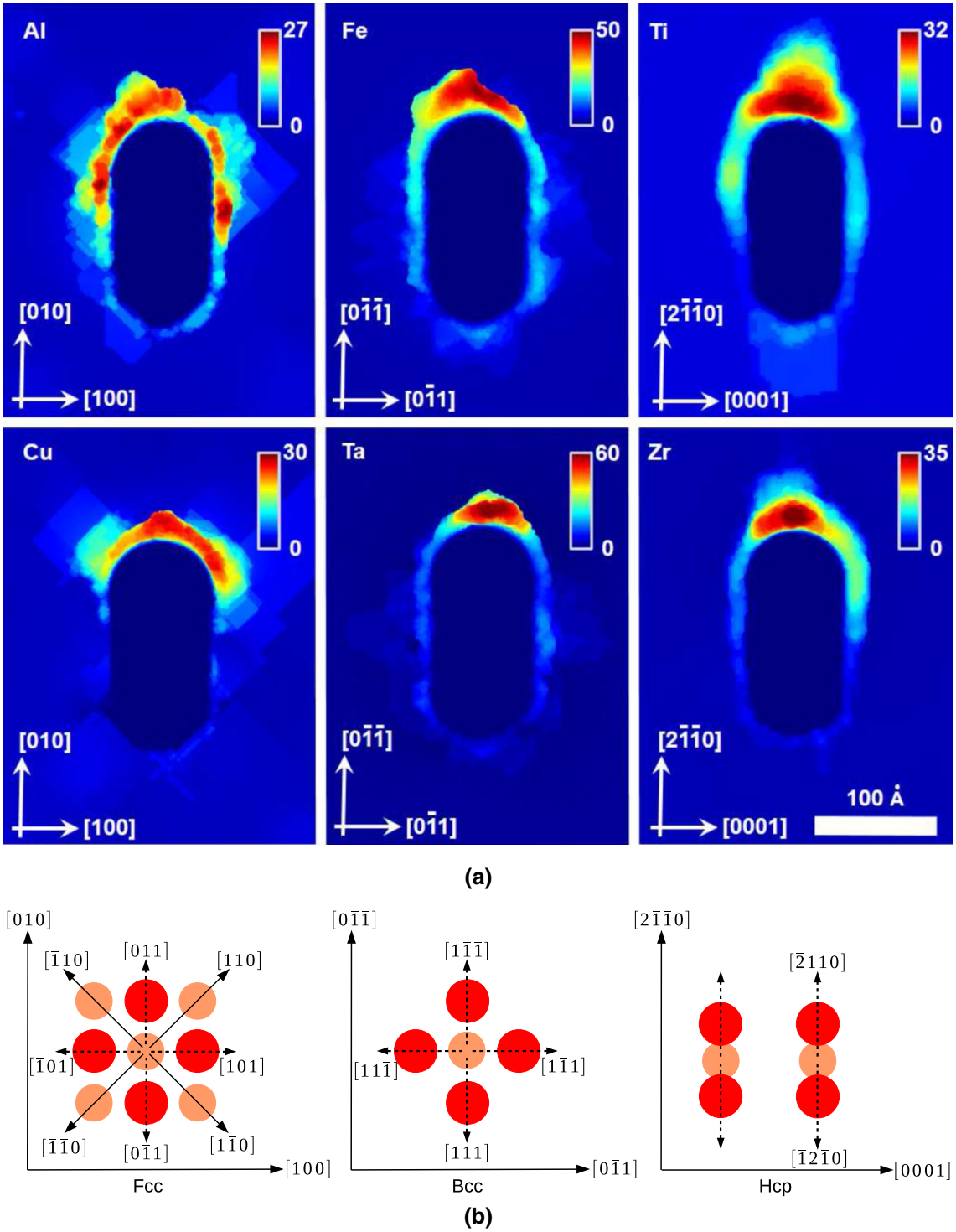

Fig. 7 **a** Synopsis of the scratch grooves and pileups generated for the six metals investigated. The color denotes the height (in Å) of the pileup above the original surface. **b** Schematics of slip systems relevant for our scratch geometry in the fcc (left), bcc (middle) and hcp (right) crystals. Full arrows are within the surface plane; dashed arrows are oblique to it. Red circles denote the first-layer atoms and orange circles second-layer atoms

Table 5 Influence of the scratch depth d on the radius of plastic zone, R_{pl}, and the plastic zone size factor, f

Crystal	d (nm)	After indent		After scratch		After retraction	
		R_{pl} (Å)	f	R_{pl} (Å)	f	R_{pl} (Å)	f
Al	2	104	2.6	134	3.4	64	1.6
	3	119	2.6	124	2.7	123	2.7
	4	145	3.0	198	4.0	174	3.6
Fe	2	74	1.9	76	1.9	74	1.9
	3	102	2.2	108	2.4	109	2.4
	4	160	3.3	130	2.7	127	2.6
Ti	2	72	1.8	72	1.8	41	1.0
	3	110	2.4	78	1.7	25	0.5
	4	156	3.2	169	3.4	134	2.7

the total length of the dislocations created in the network adherent to the groove, L_{disl}^{adh}, quantifies the plasticity.

We find that the plastic zone radii after scratch are comparable to those after indent. Due to dislocation reactions, the dislocation networks simplify, reducing the total length of dislocations. As a consequence, the average dislocation density in the plastic zone stays roughly constant.

Individually we find exceptions from this simple picture. Fcc metals show strong plastic activity, which even increases during scratch. The hcp metals on the other side show the least plastic activity. Here the plasticity may be strongly reduced during scratch and particularly during tip withdrawal.

Future work will attempt to generalize these findings to include more scratch systems. Orientations, where lateral pileup rather than frontal pileup is predominantly produced, will be particularly interesting in order to supplement our present study. In addition, our results on the size of plastic zones can be used for multi-scale modeling approaches of scratching such as the approach detailed in Ref. [50].

Acknowledgements IAA and HMU acknowledge support by the Deutsche Forschungsgemeinschaft via the Sonderforschungsbereich 926. CJR acknowledges support by ANPCyT PICT-2015-0342, SECTyP-UNCuyo, a donation by the Nvidia Corporation, and computational resources at Mendieta-CCAD-UNC through MinCyT-PDC-SNCAD.

Appendix 1: Depth Dependence of Scratching

Besides the surface orientation and the scratch direction, scratching also depends on the scratching depth d. This quantity has been fixed to 3 nm in the main part of the work. In this Appendix, we vary it between $d = 2$ and 4 nm; however, we provide the results only for one fcc metal (Al), one bcc metal (Fe), and one hcp metal (Ti).

The results are summarized in Table 5. The results are quite consistent for the fcc and bcc materials. With increasing depth d, the size factor f increases. This increase is most pronounced for the hard material, Fe, and less dramatic for Al. We attribute this increase to the effects of dislocation mobility, which is influenced by cross-slip and the details of the stress field acting under the tip [51, 52]. In addition, the results after indent also apply in good approximation for the scratch, and the removal of the tip after scratch has only a minor influence on f. These latter assertions only fail for the most shallow scratch in Al.

For the hcp material, Ti, the scratch depth plays a larger role. For the two shallowest indents, $d = 2$ and 3 nm, the plastic zone is relatively small, and almost collapses after removal of the tip, resulting in $f = 1$ or even smaller. However, more stable results are obtained for the deepest indent, $d = 4$ nm. For this depth, the resulting f factor is around 3, in good agreement with the bcc results. Only the fcc size factor is larger for this scratch depth, around $f = 4$.

We conclude that for hcp materials, shallow indents and scratches tend to lose their plastic zones by dislocation annihilation at the surface. A similar result was obtained previously for too small tip sizes [6]. Deeper indents are needed to keep the plasticity surviving.

References

1. Johnson, K.L.: Contact Mechanics. Cambridge University Press, Cambridge (1985)
2. Fischer-Cripps, A.C.: Nanoindentation, 2nd edn. Springer, New York (2004)
3. Durst, K., Backes, B., Göken, M.: Indentation size effect in metallic materials: correcting for the size of the plastic zone. Scr. Mater. **52**, 1093–1097 (2005)
4. Ruestes, C.J., Bringa, E.M., Gao, Y., Urbassek, H.M.: Molecular dynamics modeling of nanoindentation. In: Tiwari, A., Natarajan, S. (eds.) Appl. Nanoindentation Adv. Mater., pp. 313–345. Wiley, Chichester, UK (2017). **(Chap. 14)**
5. Gao, Y., Ruestes, C.J., Tramontina, D.R., Urbassek, H.M.: Comparative simulation study of the structure of the plastic zone produced by nanoindentation. J. Mech. Phys. Solids **75**, 58–75 (2015)
6. Alabd Alhafez, I., Ruestes, C.J., Gao, Y., Urbassek, H.M.: Nanoindentation of hcp metals: a comparative simulation study of the

evolution of dislocation networks. Nanotechnology **27**, 045706 (2016)
7. Komanduri, R., Chandrasekaran, N., Raff, L.M.: MD simulation of indentation and scratching of single crystal aluminum. Wear **240**, 113–143 (2000)
8. Mulliah, D., Christopher, D., Kenny, S.D., Smith, R.: Nanoscratching of silver (100) with a diamond tip. Nucl. Instrum. Methods B **202**, 294–299 (2003)
9. Mulliah, D., Kenny, S.D., Smith, R., Sanz-Navarro, C.F.: Molecular dynamic simulations of nanoscratching of silver (100). Nanotechnology **15**, 243–249 (2004)
10. Jun, S., Lee, Y., Kim, S.Y., Im, S.: Large-scale molecular dynamics simulations of Al(111) nanoscratching. Nanotechnology **15**, 1169–1174 (2004)
11. Fang, T.-H., Liu, C.-H., Shen, S.-T., Prior, S.D., Ji, L.-W., Wu, J.-H.: Nanoscratch behavior of multi-layered films using molecular dynamics. Appl. Phys. A **90**, 753–758 (2008)
12. Zhang, J.J., Sun, T., Hartmaier, A., Yan, Y.D.: Atomistic simulation of the influence of nanomachininginduced deformation on subsequent nanoindentation. Comput. Mater. Sci. **59**, 14–21 (2012)
13. Mulliah, D., Kenny, S.D., McGee, E., Smith, R., Richter, A., Wolf, B.: Atomistic modelling of ploughing friction in silver, iron and silicon. Nanotechnology **17**, 1807–1818 (2006)
14. Lu, C., Gao, Y., Michal, G., Zhu, H., Huynh, N.N., Tieu, A.K.: Molecular dynamic simulation of effect of crystallographic orientation on nano-indentation/scratching behaviors of bcc iron. In: Luo, J., Meng, Y., Shao, T., Zhao, Q. (eds.) Adv. Tribol., pp. 562–563. Springer, Berlin (2010)
15. Gao, Y., Ruestes, C.J., Urbassek, H.M.: Nanoindentation and nanoscratching of iron: atomistic simulation of dislocation generation and reactions. Comput. Mater. Sci. **90**, 232–240 (2014)
16. Gao, Y., Brodyanski, A., Kopnarski, M., Urbassek, H.M.: Nanoscratching of iron: a molecular dynamics study of the influence of surface orientation and scratching direction. Comput. Mater. Sci. **103**, 77–89 (2015)
17. Alabd Alhafez, I., Brodyanski, A., Kopnarski, M., Urbassek, H.M.: Influence of tip geometry on nanoscratching. Tribol. Lett. **65**, 26 (2017)
18. Alabd Alhafez, I., Urbassek, H.M.: Scratching of hcp metals: a molecular-dynamics study. Comput. Mater. Sci. **113**, 187–197 (2016)
19. Mendelev, M.I., Kramer, M.J., Becker, C.A., Asta, M.: Analysis of semi-empirical interatomic potentials appropriate for simulation of crystalline and liquid Al and Cu. Philos. Mag. **88**, 1723–1750 (2008)
20. Mishin, Y., Mehl, M.J., Papaconstantopoulos, D.A., Voter, A.F., Kress, J.D.: Structural stability and lattice defects in copper: Ab initio, tight-binding, and embedded-atom calculations. Phys. Rev. B **63**, 224106 (2001)
21. Mendelev, M.I., Han, S., Srolovitz, D.J., Ackland, G.J., Sun, D.Y., Asta, M.: Development of new interatomic potentials appropriate for crystalline and liquid iron. Philos. Mag. **83**, 3977–3994 (2003)
22. Dai, X.D., Kong, Y., Li, J.H., Liu, B.X.: Extended Finnis–Sinclair potential for bcc and fcc metals and alloys. J. Phys. Condens. Matter **18**, 4527–4542 (2006)
23. Mendelev, M.I., Underwood, T.L., Ackland, G.J.: Development of an interatomic potential for the simulation of defects, plasticity, and phase transformations in titanium. J. Chem. Phys. **145**, 154102 (2016)
24. Bertolino, G., Ruda, M., Pasianot, R., Farkas, D.: Atomistic simulation of the tension/compression response of textured nanocrystalline HCP Zr. Comput. Mater. Sci. **130**, 172–182 (2017)
25. Pasianot, R.C., Monti, A.M.: A many body potential for α-Zr. Application to defect properties. J. Nucl. Mater. **264**, 198–205 (1999)
26. Shao, S., Medyanik, S.N.: Dislocation-interface interaction in nanoscale fcc metallic bilayers. Mech. Res. Commun. **37**, 315–319 (2010)
27. Yaghoobi, M., Voyiadjis, G.Z.: Effect of boundary conditions on the MD simulation of nanoindentation. Comput. Mater. Sci. **95**, 626–636 (2014)
28. Voyiadjis, G.Z., Yaghoobi, M.: Large scale atomistic simulation of size effects during nanoindentation: dislocation length and hardness. Mater. Sci. Eng. A **634**, 20–31 (2015)
29. Ziegenhain, G., Urbassek, H.M., Hartmaier, A.: Influence of crystal anisotropy on elastic deformation and onset of plasticity in nanoindentation: a simulational study. J. Appl. Phys. **107**, 061807 (2010)
30. Alcalá, J., Dalmau, R., Franke, O., Biener, M., Biener, J., Hodge, A.: Planar defect nucleation and annihilation mechanisms in nanocontact plasticity of metal surfaces. Phys. Rev. Lett. **109**, 075502 (2012)
31. Ruestes, C.J., Stukowski, A., Tang, Y., Tramontina, D.R., Erhart, P., Remington, B.A., Urbassek, H.M., Meyers, M.A., Bringa, E.M.: Atomistic simulation of tantalum nanoindentation: effects of indenter diameter, penetration velocity, and interatomic potentials on defect mechanisms and evolution. Mater. Sci. Eng. A **613**, 390–403 (2014)
32. Li, J., Fang, Q., Liu, Y., Zhang, L.: A molecular dynamics investigation into the mechanisms of subsurface damage and material removal of monocrystalline copper subjected to nanoscale high speed grinding. Appl. Surf. Sci. **303**, 331–343 (2014)
33. Li, J., Liu, B., Luo, H., Fang, Q., Liu, Y., Liu, Y.: A molecular dynamics investigation into plastic deformation mechanism of nanocrystalline copper for different nanoscratching rates. Comput. Mater. Sci. **118**, 66–76 (2016)
34. Kelchner, C.L., Plimpton, S.J., Hamilton, J.C.: Dislocation nucleation and defect structure during surface indentation. Phys. Rev. B **58**, 11085–11088 (1998)
35. Ziegenhain, G., Hartmaier, A., Urbassek, H.M.: Pair vs many-body potentials: influence on elastic and plastic behavior in nanoindentation of fcc metals. J. Mech. Phys. Solids **57**, 1514–1526 (2009)
36. Plimpton, St.: Fast parallel algorithms for short-range molecular dynamics. J. Comput. Phys. **117**, 1–19 (1995). http://lammps.sandia.gov/
37. Stukowski, A.: Visualization and analysis of atomistic simulation data with OVITO—the Open Visualization Tool, Model. Simul. Mater. Sci. Eng. **18**, 015012 (2010). http://www.ovito.org/
38. Henderson, A.: Paraview guide, a parallel visualization application. Kitware Inc. (2007). http://www.paraview.org
39. Stukowski, A., Albe, K.: Extracting dislocations and non-dislocation crystal defects from atomistic simulation data. Model. Simul. Mater. Sci. Eng. **18**, 085001 (2010)
40. Stukowski, A., Bulatov, V.V., Arsenlis, A.: Automated identification and indexing of dislocations in crystal interfaces. Model. Simul. Mater. Sci. Eng. **20**, 085007 (2012)
41. Stukowski, A.: Structure identification methods for atomistic simulations of crystalline materials. Model. Simul. Mater. Sci. Eng. **20**, 045021 (2012)
42. Stukowski, A., Arsenlis, A.: On the elastic-plastic decomposition of crystal deformation at the atomic scale. Model. Simul. Mater. Sci. Eng. **20**, 035012 (2012)
43. Bowden, F.P., Tabor, D.: Friction, lubrication and wear: a survey of work during the last decade. Br. J. Appl. Phys. **17**, 1521–1544 (1966)
44. Tsuru, T., Kaji, Y., Shibutani, Y.: Minimum energy motion and core structure of pure edge and screw dislocations in aluminum. J. Comput. Sci. Tech. **4**, 185–193 (2010)

45. Muzyk, M., Pakiela, Z., Kurzydlowski, K.J.: Ab initio calculations of the generalized stacking fault energy in aluminium alloys. Scr. Mater. **64**, 916–918 (2011)
46. Monnet, G., Terentyev, D.: Structure and mobility of the $\frac{1}{2}\langle 111\rangle\{112\}$ edge dislocation in BCC iron studied by molecular dynamics. Acta Mater. **57**, 1416–1426 (2009)
47. Hafez Haghighat, S.M., von Pezold, J., Race, C.P., Körmann, F., Friak, M., Neugebauer, J., Raabe, D.: Influence of the dislocation core on the glide of the $\frac{1}{2}\langle 111\rangle\{110\}$ edge dislocation in bcc-iron. Comput. Mater. Sci. **87**, 274–282 (2014)
48. Remington, T.P., Ruestes, C.J., Bringa, E.M., Remington, B.A., Lu, C.H., Kad, B., Meyers, M.A.: Plastic deformation in nanoindentation of tantalum: A new mechanism for prismatic loop formation. Acta Mater. **78**, 378–393 (2014)
49. Tenckhoff, E.: Deformation Mechanisms, Texture, and Anisotropy in Zirconium and Zircaloy, ASTM Special Technical Publication, vol. 966. ASTM International, Philadelphia (1988)
50. Gunkelmann, N., Alabd Alhafez, I., Steinberger, D., Urbassek, H.M., Sandfeld, S.: Nanoscratching of iron: a novel approach to characterize dislocation microstructures. Comput. Mater. Sci. **135**, 181–188 (2017)
51. Po, G., Cui, Y., Rivera, D., Cereceda, D., Swinburne, T.D., Marian, J., Ghoniem, N.: A phenomenological dislocation mobility law for bcc metals. Acta Mater. **119**, 123–135 (2016)
52. Dezerald, L., Rodney, D., Clouet, E., Ventelon, L., Willaime, F.: Plastic anisotropy and dislocation trajectory in bcc metals. Nat. Commun. **7**, 11695 (2016)